




Cite this: *CrystEngComm*, 2019, 21, 3605

A novel red-emitting $\text{La}_2\text{CaHfO}_6:\text{Mn}^{4+}$ phosphor based on double perovskite structure for pc-WLEDs lighting†

Gongcheng Xing,^a Yuxin Feng,^a Zhiyu Gao,^a Mengxuan Tao,^a Hongquan Wang,^{*a} Yi Wei,^a Maxim S. Molokeev ^{bcd} and Guogang Li^{*a}

Non-rare earth doped oxides with red emission are one of the current research hotspots for achieving the warm white light range in the phosphor converted white light emitting diodes (pc-WLEDs) field. In the current work, a novel Mn^{4+} -activated $\text{La}_2\text{CaHfO}_6$ red phosphor is reported for the first time and its crystal structure is analyzed by Rietveld refinement. The photoluminescent properties of $\text{La}_2\text{CaHfO}_6:\text{Mn}^{4+}$ are investigated in detail with the help of diffuse reflectance spectroscopy, photoluminescence spectroscopy, and temperature-dependent PL spectroscopy. Based on the diffuse reflectance spectra, the calculated optical band gap for $\text{La}_2\text{CaHfO}_6$ is 4.9 eV, indicating that $\text{La}_2\text{CaHfO}_6$ could be a suitable host for activators' doping. Under 380 nm near-ultraviolet (n-UV) light excitation, the as-prepared $\text{La}_2\text{CaHfO}_6:\text{Mn}^{4+}$ displays intense red emission centered at 693 nm. Through an accurate calculation of Dq/B (2.47) and nephelauxetic effect β_1 (0.949), the origination of strong crystal field (CF) and deep-red emission is demonstrated. By combining the representative $\text{La}_2\text{CaHfO}_6:0.002\text{Mn}^{4+}$, blue $\text{BAM}:\text{Eu}^{2+}$, and green $(\text{Ba,Sr})_2\text{SiO}_4:\text{Eu}^{2+}$ phosphors with a 380 nm UV chip to fabricate the pc-WLEDs device, a white light is obtained with low correlated color temperature (CCT = 5165 K) and high color rendering index (Ra = 87.8), demonstrating that the as-prepared $\text{La}_2\text{CaHfO}_6:\text{Mn}^{4+}$ phosphors can be used as red-emitting candidate in pc-WLEDs lighting.

Received 13th April 2019,
Accepted 9th May 2019

DOI: 10.1039/c9ce00556k

rs.li/crystengcomm

1. Introduction

Phosphor-converted white light-emitting diodes (pc-WLEDs) have been considered as the most promising solid state lighting sources due to their high luminous efficiency, low energy costs, and excellent stability.^{1–3} The commercial pc-WLEDs are a combination of blue LED chip (InGaN) and the famous yellow phosphor (YAG:Ce³⁺).⁴ However, some technical weaknesses appear in their practical application due to the lack of a red-emitting component, which usually generates high correlated color temperature (CCT) and low color rendering index (CRI) for the white light.^{5,6} Therefore, this combination

is harmful to human eyes in long term indoor illumination.^{7–9} In order to solve the above problems, a red-emitting phosphor is urgently needed.

Previously, commercial red luminescence materials used were composed of rare-earth ions Ce³⁺ and Eu²⁺ doped nitrides such as $\text{M}_2\text{Si}_5\text{N}_8:\text{Ce}^{3+}$ (M = Ca, Sr, Ba),¹⁰ $\text{CaAlSiN}_3:\text{Eu}^{2+}$,¹¹ and $\text{Ca}_2\text{Si}_5\text{N}_8:\text{Eu}^{2+}$,¹² which display superior thermal stability and high quantum yield (QY > 90%). Nevertheless, the harsh synthetic conditions (high temperature > 2000 K and high pressure > 1 MPa) and expensive cost make it difficult to achieve their large-scale indoor lighting applications. Recently, Mn^{4+} -doped red-emitting phosphors have attracted much attention in the improvement of the lighting quality of pc-WLEDs, in which Mn^{4+} ions usually occupy the octahedral coordination environment and exhibit narrow-band emission.^{13,14} A range of $\text{A}_2\text{MF}_6:\text{Mn}^{4+}$ (A = alkali metal ion, M = Si, Ge, Ti) fluoride phosphors have been considered as promising candidates for pc-WLEDs and display lighting.^{15–17} They possess broad excitation band ranging from n-UV to blue region, which matches well with the n-UV or blue LED chip. Due to intense and narrow red emission, $\text{A}_2\text{MF}_6:\text{Mn}^{4+}$ fluoride phosphors generally have high QY. For instance, the QY of $\text{K}_2\text{TiF}_6:\text{Mn}^{4+}$ is up to 98%, which is the highest value compared to previously reported red phosphors.¹⁸ However, the use of corrosive and toxic hydrofluoric acid during the preparation and

^a Engineering Research Center of Nano-Geomaterials of Ministry of Education, Faculty of Materials Science and Chemistry, China University of Geosciences, 388 Lumo Road, Wuhan 430074, P. R. China. E-mail: ggli@cug.edu.cn, wanghq@cug.edu.cn

^b Laboratory of Crystal Physics, Kirensky Institute of Physics, FRC KSC SB RAS, Krasnoyarsk 660036, Russia

^c Department of Physics, Far Eastern State Transport University, Khabarovsk, 680021, Russia

^d Siberian Federal University, Krasnoyarsk, 660041, Russia

† Electronic supplementary information (ESI) available. See DOI: 10.1039/c9ce00556k

poor moisture resistance are constraints in its practical application.

Due to their superior chemical stability and eco-friendly preparation procedure, Mn^{4+} -doped oxides such as $\text{CaAl}_{12}\text{O}_{19}:\text{Mn}^{4+}$,¹⁹ $\text{Sr}_4\text{Al}_{14}\text{O}_{25}:\text{Mn}^{4+}$,²⁰ and $\text{CaMg}_2\text{Al}_{16}\text{O}_{27}:\text{Mn}^{4+}$ (ref. 21) have attracted more and more attention. They show promising capabilities as the excellent red components in pc-WLEDs. Because they possess two types octahedral sites (B and B' sites), some double perovskite structures ($\text{A}_2\text{BB}'\text{O}_6$) are appropriate hosts for Mn^{4+} -doping.^{22,23} Previously, a series of Mn^{4+} -doped double perovskite structured phosphors have been reported, for example, $\text{Ba}_2\text{GdNbO}_6:\text{Mn}^{4+}$,²⁴ $\text{Gd}_2\text{ZnTiO}_6:\text{Mn}^{4+}$,²⁵ $\text{Li}_2\text{MgZrO}_4:\text{Mn}^{4+}$,²⁶ $\text{NaMgGdTeO}_6:\text{Mn}^{4+}$,²⁷ $\text{Sr}_2\text{LaNbO}_6:\text{Mn}^{4+}$,²⁸ $\text{Sr}_2\text{ZnMoO}_6:\text{Mn}^{4+}$,²⁹ and $\text{Sr}_2\text{ZnWO}_6:\text{Mn}^{4+}$.³⁰ However, the luminescent properties of the prepared phosphors are not satisfactory, and further optimization and improvement as well as the exploration of new double perovskite structures for Mn^{4+} -doping is needed.

In this work, we have reported for the first time a novel red-emitting double perovskite structured $\text{La}_2\text{CaHfO}_6:\text{Mn}^{4+}$ phosphor, prepared *via* a transitional high-temperature solid state reaction. The crystal structure has been analyzed through the Rietveld refinement method. The luminescence properties including photoluminescence, temperature-dependence luminescence, and fluorescence lifetimes of the as-prepared phosphors have been investigated in detail. The luminous mechanism has been explained by the Tanabe–Sugano energy-level diagram of Mn^{4+} . Finally, the electroluminescence (EL) performance of the fabricated pc-WLEDs device by combining $\text{La}_2\text{CaHfO}_6:\text{Mn}^{4+}$, $\text{BAM}:\text{Eu}^{2+}$, and $(\text{Ba}, \text{Sr})_2\text{SiO}_4:\text{Eu}^{2+}$ phosphors with a 380 nm n-UV chip has been discussed, demonstrating that the as-prepared $\text{La}_2\text{CaHfO}_6:\text{Mn}^{4+}$ phosphor could be considered as a red-emitting candidate in pc-WLEDs lighting.

2. Experimental

2.1 Synthesis

The $\text{La}_2\text{CaHf}_{1-x}\text{O}_6:x\text{Mn}^{4+}$ ($0.0005 \leq x \leq 0.01$) (abbreviated as $\text{LCH}:x\text{Mn}^{4+}$) was prepared by high-temperature solid state method in air. The original materials La_2O_3 , CaCO_3 , HfO_2 , and MnCO_3 with a purity of 99.99% were weighed in the designed stoichiometric molar ratio. After grinding for 30 min in an agate mortar, the mixture was put into alumina crucibles and sintered in a tube furnace at 1500 °C for 10 h. Finally, all the samples were successfully prepared by grinding again after cooling to room temperature naturally.

2.2 Device fabrication

The pc-WLEDs devices were fabricated by combining the mixture of commercially available blue $\text{BAM}:\text{Eu}^{2+}$, green $(\text{Ba}, \text{Sr})_2\text{SiO}_4:\text{Eu}^{2+}$, and representative $\text{LCH}:0.002\text{Mn}^{4+}$ phosphors with 380 nm InGaN chips. Then, the proper amounts of the mixture were added into epoxy resins and mixed thoroughly for 20 min. The acquired mixture was coated on the surface of the 380 nm InGaN chips and dried at 120 °C to produce

the pc-WLEDs. All measurements were carried out at 20 mA driven current.

2.3 Characterization

The X-ray diffraction (XRD) data for determining the phase purity and crystal structure of the as-prepared samples were obtained by using a D8 Focus diffractometer at a scanning rate of 1° min^{-1} in the 2θ range from 10° to 120° with Ni-filtered $\text{Cu K}\alpha$ ($\lambda = 1.540598 \text{ \AA}$). The Rietveld profile refinements of the structural models and texture analysis were done using the General Structure Analysis System (GSAS) software. The morphologies, energy-dispersive X-ray spectra (EDS), and elemental mapping of the samples were obtained using a field emission scanning electron microscope (FE-SEM, S-4800, Hitachi). The diffuse reflectance spectra (DRS) were recorded on a UV-visible diffuse reflectance spectrophotometer UV-2550PC (Shimadzu Corporation, Japan). The photoluminescence excitation (PLE) and emission (PL) spectra were obtained on a fluorescence spectrometer (Fluoromax-4P, Horiba Jobin Yvon, New Jersey, U.S.A.) equipped with a 150 W xenon lamp as the excitation source, and both the excitation and emission spectra were obtained with the width of the monochromator slits adjusted to 1.0 nm. The lifetimes of the as-prepared samples were determined by a Lecroy Wave Runner 6100 Digital Oscilloscope (1 GHz) using a tunable laser (pulse width = 4 ns; gate = 50 ns) as the excitation source (Continuum Sunlite OPO). The thermal stabilities of the luminescence properties were studied on a Fluoromax-4P spectrometer using a combined setup consisting of a Xe lamp, a Hamamatsu MPCD-7000 multichannel photodetector, and a computer-controlled heater (TAP-02). Commission Internationale de l'Eclairage chromaticity color coordinates, color rendering index (CRI), and corresponding color temperatures (CCT) of the WLEDs devices were measured by using an integrating sphere with an analyzer system (tarspec SSP6612).

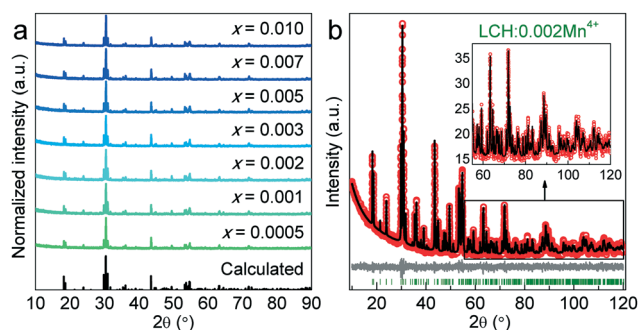


Fig. 1 (a) XRD patterns of $\text{LCH}:x\text{Mn}^{4+}$ ($0.0005 \leq x \leq 0.01$) samples and calculated standard data of LCH. (b) Rietveld refinement XRD data of the representative $\text{LCH}:0.002\text{Mn}^{4+}$ sample with the measured data (red circle), fitted data (black line), difference (grey line), and Bragg position (olive vertical bar).

3. Results and discussion

3.1 Phase purity and crystal structure identification

A novel Mn⁴⁺-doped La₂CaHfO₆ (abbreviated as LCH) double perovskite phosphor was successfully synthesized by a high-temperature solid state reaction. As given in Fig. 1a, the XRD patterns of LCH:xMn⁴⁺ could be well indexed to the calculated La₂CaHfO₆ peaks, according to previous reports.^{31,32} There is no evident impurity phase, indicating the formation of a pure phase for the LCH:xMn⁴⁺ samples and the successful doping of Mn⁴⁺ ions into the LCH host. In order to determine the structural features of LCH:xMn⁴⁺, the powder XRD data of the representative LCH:0.002Mn⁴⁺ were collected at room temperature with 2θ range from 10° to 120° for Rietveld refinement analysis. The experimental (red circle) and calculated (black line) XRD profiles together with their difference (grey line) for LCH:0.002Mn⁴⁺ are exhibited in Fig. 1b. The refinement is well-convergent due to the low *R*-factors *R*_p = 5.77% and *R*_{wp} = 4.43%, which demonstrates that stable and pure samples were obtained. The final refinement results and main parameters of processing are presented in Table 1. On the basis of the refinement results, LCH:xMn⁴⁺ belongs to the monoclinic (*P*_{2₁}/*n*) group and the main lattice parameters of the representative sample LCH:0.002Mn⁴⁺ are *a* = 5.77510 Å, *b* = 5.98686 Å, *c* = 8.30488 Å, and *V* = 287.138 Å³. LCH:xMn⁴⁺ presents a typical double perovskite structure (A₂BB'O₆), where A sites, B sites, and B' sites are occupied by La atoms, Ca atoms, and Hf atoms, respectively. The main bond lengths in the LCH:0.002Mn⁴⁺ sample are summarized in Table 2. Moreover, a schematic crystal structure of LCH:xMn⁴⁺ is shown in Fig. 2. There is only one type of La, Ca, and Hf site. The [CaO₆] octahedron is involved in vertex-sharing with the [HfO₆] octahedron and the La atoms located at the lattice spacing form the [LaO₇] polyhedron that is involved in vertex-sharing with [CaO₆] or [HfO₆] octahedron. In the LCH:xMn⁴⁺ system, there are three cationic sites for Mn⁴⁺ occupation. However, considering the charge valence (+4) and similar ionic radius of La³⁺ (*r* = 1.1 Å, CN = 7), Ca²⁺ (*r* = 1 Å, CN = 6), Hf⁴⁺ (*r* = 0.71 Å, CN = 6), and Mn⁴⁺ (*r* = 0.53 Å, CN = 6),³³ the Hf⁴⁺ site is considered as the most suitable cationic site for Mn⁴⁺ ions.

Table 1 Main crystallographic parameters in the processing and refinement of the LCH:0.002Mn⁴⁺ sample structure

Compound	La ₂ CaHfO ₆ :0.002Mn ⁴⁺
Sp.Gr.	<i>P</i> _{2₁} / <i>n</i>
<i>a</i> , Å	5.77510 (6)
<i>b</i> , Å	5.98686 (6)
<i>c</i> , Å	8.30488 (8)
β, °	90.1564 (6)
<i>V</i> , Å ³	287.138 (5)
<i>Z</i>	2
<i>R</i> _{wp} , %	5.77
<i>R</i> _p , %	4.43
<i>R</i> _{exp} , %	4.52
χ ²	1.28
<i>R</i> _B , %	1.74

Table 2 Main bond lengths (Å) in the LCH:0.002Mn⁴⁺ sample

Bond	Length (Å)	Bond	Length (Å)
La–O1 ⁱ	2.930 (16)	Ca–O1 ⁱ	2.345 (15)
La–O1 ⁱⁱ	2.288 (16)	Ca–O2	2.353 (15)
La–O1 ⁱⁱⁱ	2.849 (15)	Ca–O3 ^{vi}	2.388 (14)
La–O2	2.485 (12)	Hf–O1 ⁱ	2.094 (14)
La–O2 ^{iv}	2.391 (12)	Hf–O2 ^{iv}	2.039 (15)
La–O3 ⁱⁱ	2.731 (15)	Hf–O3 ⁱ	1.986 (15)
La–O3 ^v	2.471 (15)	—	—

Symmetry codes: (i) *x*, *y*, *z* – 1; (ii) –*x* + 1, –*y* + 1, –*z* + 1; (iii) *x* + 1/2, –*y* + 1/2, *z* – 1/2; (iv) –*x* + 1/2, *y* + 1/2, –*z* + 1/2; (v) *x* + 1/2, –*y* + 3/2, *z* – 1/2; (vi) *x*, *y* – 1, *z* – 1.

To further confirm the successful incorporation of Mn⁴⁺ ions into LCH, SEM images and corresponding elemental maps of La, Ca, Hf, O, and Mn in LCH:0.002Mn⁴⁺ were obtained and are exhibited in Fig. 3. On the basis of the SEM image, it can be observed that the as-prepared sample is composed of irregular particles of about 5–10 μm diameter. Meanwhile, La, Ca, Hf, O, and Mn elements are uniformly distributed throughout the whole viewing area. This result indicates that Mn⁴⁺ ions are successfully doped into LCH.

3.2 Luminescent properties' analysis

In order to investigate the optical properties of LCH:Mn⁴⁺ phosphors, the direct band gap (Fig. 4a) of the LCH host was calculated by the following formula:^{34–37}

$$[F(R)hv]^2 = A(hv - E_g), F(R) = (1 - R)^2/2R \quad (1)$$

where *A* stands for the absorption constant, *E_g* represents the optical band gap, *hν* is the photon energy, *F(R)* is the absorption coefficient, and *R* is the reflectance coefficient (%). The calculated value of the direct band gap was 4.9 eV, indicating that LCH is a suitable host for Mn⁴⁺-doping. The UV-vis diffuse reflectance spectra (DRS) with different Mn⁴⁺

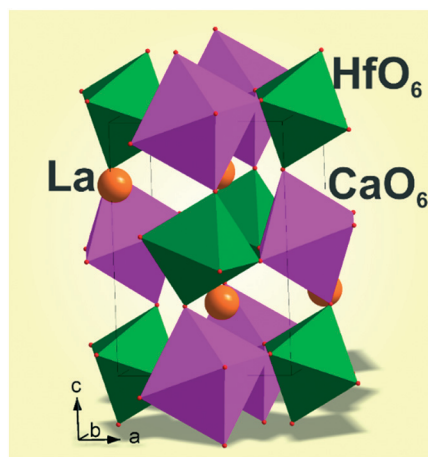


Fig. 2 A schematic crystal structure of LCH, possessing one kind of [LaO₇], [CaO₆], and [HfO₆] polyhedra.

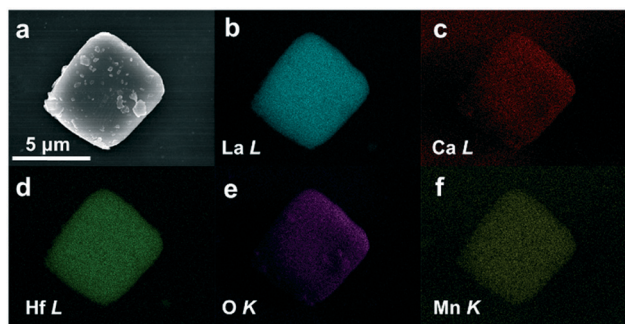


Fig. 3 (a) SEM image of LCH:0.02Mn⁴⁺. (b)–(f) Corresponding elemental maps for La, Ca, Hf, O, and Mn elements in LCH:0.02Mn⁴⁺.

concentrations ($0.0005 \leq x \leq 0.01$) are displayed in Fig. 4b. The DR spectra of all the samples consist of two distinct absorption bands. The main one is located in the region of 300 nm–480 nm, attributed to charge transfer (CT) transitions of Mn⁴⁺–O²⁻ and electron transitions from ⁴A_{2g} ground state to ⁴T_{1g} and ²T_{2g} excited states. The other one ranges from 480 nm to 600 nm, resulting from the transition from ⁴A_{2g} ground state to ⁴T_{2g} excited state. Fig. 4c displays the photoluminescence excitation (PLE) spectra of LCH:xMn⁴⁺ ($0.0005 \leq x \leq 0.01$) monitored at 693 nm. All the spectra have two obvious excitation bands, which are in good agreement with the DRS results. The major one ranges from 280 nm to 480 nm with the maximum value at 380 nm, and the weak one ranges from 480 nm to 600 nm, with its maximum centred at 525 nm. The two dominant excitation bands match well with the n-UV and blue LED chip, which implies that the as-prepared samples could be used as potential red-emitting

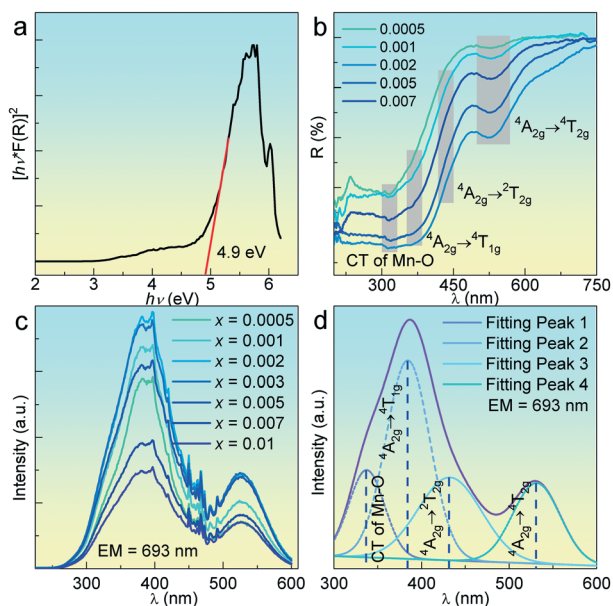


Fig. 4 (a) The relationship of $[F(R)hv]^2$ vs. photon energy hv in the LCH host. (b) Diffuse reflectance spectra corresponding to different Mn⁴⁺ concentrations (x) in LCH:xMn⁴⁺ ($0.0005 \leq x \leq 0.007$). (c) PLE spectra of LCH:xMn⁴⁺ ($0.0005 \leq x \leq 0.01$), monitored at 693 nm. (d) The Gaussian fitting of the PLE spectra of the LCH:0.002Mn⁴⁺ sample.

phosphors. The representative PLE spectrum of LCH:0.002Mn⁴⁺ was analyzed by Gaussian fitting, which is presented in Fig. 4d. There are four Gaussian fitting peaks centred at 337 nm, 384 nm, 432 nm, and 531 nm, which are attributed to the Mn⁴⁺–O²⁻ charge-transfer band and transitions from the ⁴A_{2g} ground state to the ⁴T_{1g}, ²T_{2g}, and ⁴T_{2g} excited states of Mn⁴⁺, respectively.

Fig. 5a shows the photoluminescence emission (PL) spectra of LCH:xMn⁴⁺ ($0.0005 \leq x \leq 0.01$) under 380 nm UV excitation. The red emission is assigned to the transitions from the ²E_g excited state to the ⁴A_{2g} ground state. It is clearly seen that no evident change occurs in the peak shape and position at different Mn⁴⁺-doping concentrations (x). The inset in Fig. 5a gives the digital images of the as-prepared LCH:0.002Mn⁴⁺ sample under daylight and 365 nm n-UV light, providing a visible evidence of the bright red emission from LCH:xMn⁴⁺. Moreover, the CIE chromaticity coordinates diagram of the representative LCH:0.002Mn⁴⁺ is displayed in Fig. 5b, where a deep-red-emission with CIE chromaticity coordinates of (0.721, 0.280) was obtained. Meanwhile, the PL intensity increases gradually with Mn⁴⁺ concentration (x) until it reaches a maximum at $x = 0.002$, then it decreases on further increasing the Mn⁴⁺ concentration (x) (Fig. 5c) due to a concentration quenching effect. Generally, with the increase in the Mn⁴⁺ concentration (x), the adjacent Mn⁴⁺ ions become closer, which increases the possibility of energy transfer among the nearest Mn⁴⁺ ions. Hence, the distance between adjacent Mn⁴⁺ ions will determine the concentration

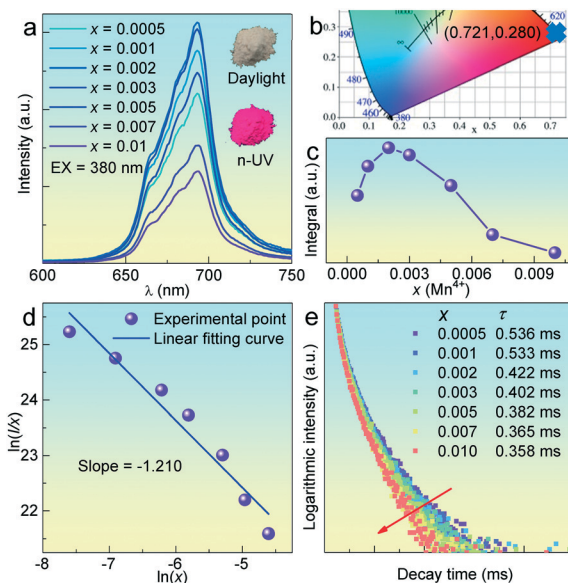


Fig. 5 (a) PL spectra of LCH:xMn⁴⁺ ($0.0005 \leq x \leq 0.01$), the insets are luminescence photographs LCH:0.002Mn⁴⁺ in daylight (up) and in 365 nm n-UV light (down) illumination, respectively. (b) The CIE chromaticity coordinates diagram for LCH:0.002Mn⁴⁺. (c) The integrated intensity of LCH:xMn⁴⁺ ($0.0005 \leq x \leq 0.01$) as a function of Mn⁴⁺ concentration (x). (d) The dependence of $\ln(I/x)$ on $\ln(x)$ for LCH:xMn⁴⁺ ($0.0005 \leq x \leq 0.01$). (e) The corresponding PL decay curves of LCH:xMn⁴⁺ ($0.0005 \leq x \leq 0.01$) monitored at 693 nm excitation at 380 nm.

quenching. The critical distance (R_c) can be calculated by the following formula:^{38,39}

$$R_c = 2 \left[\frac{3V}{4\pi x_c N} \right]^{\frac{1}{3}} \quad (2)$$

where V represents the cell volume, x_c stands for the critical concentration of Mn^{4+} , and N is the number of dopant sites available per unit cell. In $\text{LCH}:x\text{Mn}^{4+}$, $V = 287.138 \text{ \AA}^3$, $x_c = 0.002$, and $N = 2$. The calculated R_c value is 25.78 \AA , which is much larger than 5 \AA . Therefore, electric multipolar interaction is responsible for the quenching mechanism in Mn^{4+} -doped LCH phosphor. Furthermore, the type of electric multipolar interaction can be obtained from the following eqn:³⁹

$$\frac{I}{x} = K \left[1 + \beta(x)^{\frac{\theta}{3}} \right]^{-1} \quad (3)$$

where I is the PL intensity of $\text{LCH}:x\text{Mn}^{4+}$, x represents the concentrations of Mn^{4+} , K and β are constants at the same excitation conditions and host lattice. $\theta = 6, 8, \text{ and } 10$ represent the dipole–dipole, dipole–quadrupole, and quadrupole–quadrupole interactions, respectively. Fig. 5d shows the relationship between $\ln(x)$ and $\ln(I/x)$. It can be well-fitted by straight line with a slope of -1.21 ($-\theta/3$). The calculated value of θ is 3.62 , which is close to 6 . This means that the dipole–dipole interaction dominates the concentration quenching mechanism in $\text{LCH}:x\text{Mn}^{4+}$.

The luminescence decay curves of $\text{LCH}:x\text{Mn}^{4+}$ are displayed in Fig. 5e (EM = 693 nm , EX = 380 nm). All of the decay curves match well with the single exponential fitting model with the following formula:

$$I_T = I_0 \exp\left(\frac{-t}{\tau}\right) \quad (4)$$

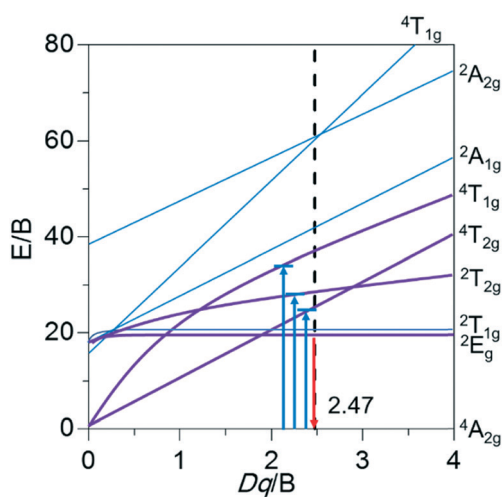


Fig. 6 Tanabe–Sugano energy-level diagram for Mn^{4+} (d^3) electron configuration in the octahedral site of the LCH host.

where I_0 and I_T represent the luminescence intensities of Mn^{4+} at t_0 and t ; τ stands for luminescence decay lifetimes for the corresponding samples. For the Mn^{4+} concentrations (x) of $0.0005, 0.001, 0.002, 0.003, 0.005, 0.007, \text{ and } 0.01$, the calculated values of decay lifetime for $\text{LCH}:x\text{Mn}^{4+}$ are $0.536, 0.533, 0.422, 0.402, 0.382, 0.365, \text{ and } 0.358 \text{ ms}$, respectively. It can be seen that the lifetime of the samples declines steadily, which is attributed to the enhancement of non-radiative energy migration among the adjacent Mn^{4+} ions with increasing Mn^{4+} concentration (x).

Generally, in the octahedral site, the luminescence mechanism of Mn^{4+} can be analyzed by the Tanabe–Sugano energy level diagram (Fig. 6). When the electrons at ${}^4\text{A}_{2g}$ ground state are excited, they are pumped to the ${}^4\text{T}_{1g}, {}^2\text{T}_{2g}, \text{ and } {}^4\text{T}_{2g}$ excited states. Thereafter, the excited electrons relax to the lowest excited state ${}^2\text{E}_g$ by non-radiative transition process. Eventually, these electrons return to the ground state from ${}^4\text{A}_{2g}$, which results in far-red light centered at 693 nm . Owing to the special $3d^3$ electron configuration, the Mn^{4+} energy level transition is easily influenced by the crystal field (CF) environment. The CF strength (Dq) can be roughly represented with the energy difference of ${}^4\text{A}_{2g} \rightarrow {}^4\text{T}_{2g}$ by the following formula:²⁵

$$Dq = E({}^4\text{A}_{2g} \rightarrow {}^4\text{T}_{2g})/10 \quad (5)$$

In addition, the Racah parameter B can be calculated from the following eqn:²⁶

$$\frac{Dq}{B} = \frac{15(\delta - 8)}{(\delta^2 - 10\delta)} \quad (6)$$

The value of δ can be calculated as follows:²⁷

$$\delta = \frac{[E({}^4\text{A}_{2g} \rightarrow {}^4\text{T}_{1g}) - E({}^4\text{A}_{2g} \rightarrow {}^4\text{T}_{2g})]}{Dq} \quad (7)$$

Moreover, the Racah parameter C can be acquired from the following eqn:⁴⁰

$$\frac{E({}^2\text{E}_g \rightarrow {}^4\text{A}_{2g})}{B} = \frac{3.05C}{B} + 7.9 - \frac{1.8B}{Dq} \quad (8)$$

According to the abovementioned PLE and PL spectra, the peak energies of ${}^4\text{A}_{2g} \rightarrow {}^4\text{T}_{1g}, {}^4\text{A}_{2g} \rightarrow {}^4\text{T}_{2g}, \text{ and } {}^2\text{E}_g \rightarrow {}^4\text{A}_{2g}$ for $\text{LCH}:0.002\text{Mn}^{4+}$ are $26052 \text{ cm}^{-1}, 23148 \text{ cm}^{-1}, \text{ and } 14437 \text{ cm}^{-1}$, respectively. The value of Dq, B , and C can be calculated from the formulas (5)–(8), which are $1887 \text{ cm}^{-1}, 765 \text{ cm}^{-1}, \text{ and } 2935 \text{ cm}^{-1}$, respectively. The calculated energy level, Dq, and Racah parameter values for $\text{LCH}:\text{Mn}^{4+}$ are given in Table 3. The Dq/B value of $\text{LCH}:0.002\text{Mn}^{4+}$ is greater than 2 (2.47), indicating that $\text{LCH}:x\text{Mn}^{4+}$ exists in a strong CF. However, the parity-forbidden ${}^2\text{E}_g \rightarrow {}^4\text{A}_{2g}$ transition is barely influenced by the CF strength and greatly affected by the nephelauxetic effect, which is highly dependent on the

Table 3 The calculated energy levels, Dq, and Racah parameter values for Mn⁴⁺

	Wavenumber (cm ⁻¹)
⁴ A _{2g} → ⁴ T _{1g}	26 052
⁴ A _{2g} → ⁴ T _{2g}	23 148
² E _g → ⁴ A _{2g}	14 437
Dq	1887
B	765
C	2935

covalence of the Mn⁴⁺ ions and the ligand. Brik *et al.* reported that the nephelauxetic effect can be described by nephelauxetic ratio (β_1) with the following formula:^{41–44}

$$\beta_1 = \sqrt{\left(\frac{B}{B_0}\right)^2 + \left(\frac{C}{C_0}\right)^2} \quad (9)$$

where B_0 and C_0 are the Racah parameters for free ions of Mn⁴⁺, ($B_0 = 1160 \text{ cm}^{-1}$ and $C_0 = 4303 \text{ cm}^{-1}$). The calculated value of β_1 is 0.9488. In a previous report,⁴⁵ the peak energy and peak position of ²E_g → ⁴A_{2g} for Mn⁴⁺ could be calculated as $E(^2E_g \rightarrow ^4A_{2g}) = -880.49 + 16261.92\beta_1 \pm \sigma$ ($\sigma = 332 \text{ cm}^{-1}$), which was obtained for a large amount of Mn⁴⁺-activated crystals that are listed in a figure and fitted by a linear relationship, and the σ stands for root-mean square (rms) deviation of the data points from the fitting line. In this case, the calculated ²E_g energy level is 14 217–14 881 cm⁻¹ and the experimental energy value for the ²E_g → ⁴A_{2g} transition of Mn⁴⁺ in the LCH:xMn⁴⁺ host was 14 437 cm⁻¹. The above result is in accordance with the linear line and thus, it is reliable.

3.3 Thermal stability properties

As the working temperature of pc-WLEDs can reach 150 °C, thermal stability is one of the most important properties for defining the lighting quality of phosphors.^{46,47} The temperature-dependent PL spectrum of LCH:0.002Mn⁴⁺ was obtained in the temperature range from room temperature (25 °C) to 200 °C, with an interval of 25 °C. As illustrated in

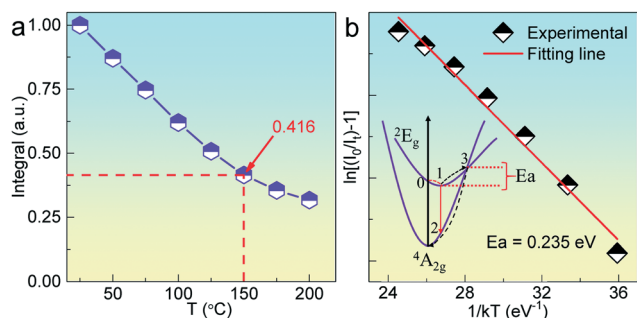


Fig. 7 (a) The integral intensity of LCH:0.002Mn⁴⁺ as a function of temperature (T , °C). (b) Arrhenius fitting of the integrated intensity in LCH:0.002Mn⁴⁺, the inset is the schematic configuration coordinate diagram for Mn⁴⁺.

Fig. 7a, the temperature-dependent PL intensity of LCH:0.002Mn⁴⁺ gradually decreases with increasing temperature. At 150 °C, the integrated intensity is only 0.416 times of that at 25 °C. This indicates that great thermal quenching occurs during the increase in temperature for LCH:xMn⁴⁺, which results from magnified population at higher vibration levels or the probability of non-radiative transfer. To better understand the process of thermal quenching, the activation energy (E_a) was calculated by the Arrhenius equation:

$$I_T = \frac{I_0}{1 + A \exp(-E_a/kT)} \quad (10)$$

where I_T and I_0 represent the integrated PL intensity at the testing temperature and room temperature, respectively, A is a constant for a certain host, and k represents the Boltzmann constant ($8.629 \times 10^{-5} \text{ eV}$). Fig. 7b displays the relationship of $\ln[(I_0/I_T)^{-1}]$ versus $1/kT$ and the calculated value of E_a is 0.235 eV. Thermal quenching can be explained by the configuration coordinate diagram (inset of Fig. 7b). At room temperature, when the electrons of the ground state ⁴A_{2g} are excited upon n-UV or blue chips, they jump to the excited states ⁴T_{1g}, ²T_{2g}, and ⁴T_{2g}, respectively, and then relax to the ²E_g level *via* non-radiative transition. Thereafter, the electrons return to the ⁴A_{2g} ground state through the path 0 → 1 → 2 with red emission. As the temperature increases, thermal excitation results in the electrons jumping to the crossover point between ²E_g and ⁴A_{2g}, thereby leading to non-radiative transition to the ground state through the path 0 → 1 → 3 → 2, which is responsible for thermal quenching. Although a serious thermal quenching was observed in LCH:xMn⁴⁺ based on the current experimental results, the thermal stability of LCH:xMn⁴⁺ could be further improved by process optimization.

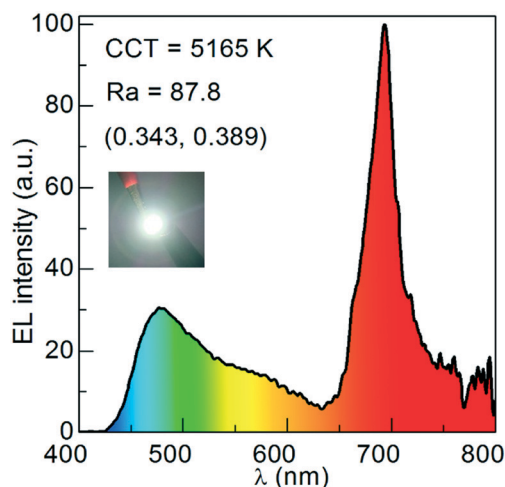


Fig. 8 Electroluminescence spectrum of the pc-WLEDs device fabricated by combination of commercial blue BAM:Eu²⁺ phosphor, green (Ba,Sr)₂SiO₄:Eu²⁺ phosphor, and the representative red LCH:0.002Mn⁴⁺ phosphor, and driven by n-UV LED chip ($\lambda = 380 \text{ nm}$). The inset is the digital photograph of the obtained pc-WLEDs device.

3.4 Electroluminescence performance of the fabricated pc-WLEDs device

To demonstrate the possibility of practical application of the as-prepared phosphor, we fabricated the pc-WLEDs device by combining n-UV LED chip ($\lambda = 380$ nm) and the mixture of commercial blue BAM:Eu²⁺ phosphor, green (Ba, Sr)₂SiO₄:Eu²⁺ phosphor, and the representative red LCH:0.002Mn⁴⁺ phosphor. The performance of the fabricated pc-WLEDs and the digital photograph are shown in Fig. 8. Under a voltage of 3.15 V and current of 20 mA, the obtained pc-WLEDs device exhibits white emission with low corresponding color temperature (CCT = 5165 K) and high CIR ($R_a = 87.8$). The CIE coordinates are located at (0.343, 0.389). These results indicate that the as-prepared LCH:0.002Mn⁴⁺ double-perovskite phosphor could be an excellent candidate as a red-emitting component for application in warm pc-WLEDs.

4. Conclusion

In summary, a novel red-emitting LCH:Mn⁴⁺ phosphor was successfully prepared by high-temperature solid state reaction. On the basis of the Rietveld refinement results, the double perovskite structured LCH:xMn⁴⁺ crystallizes in the monoclinic phase ($P2_1/n$) and the Hf⁴⁺ ions are the most suitable site for Mn⁴⁺-doping. When monitored at 693 nm, it presents a broad-band PLE spectrum from 275 nm to 600 nm, which matches well with the n-UV and blue LED chip. It implies that the as-prepared samples could be a potential red-emitting phosphor for use in pc-WLEDs. Under 380 nm or 525 nm excitation, a narrow deep-red emission located at 693 nm is obtained, which is attributed to the ²E_g → ⁴A_{2g} transitions of Mn⁴⁺. The optimized Mn⁴⁺-doping concentration (x) in the LCH host is 0.2 atom% of Hf⁴⁺. The concentration quenching is attributed to the dipole-dipole interaction. Moreover, the luminescence mechanism of LCH:xMn⁴⁺ has been analyzed in detail by the Tanabe-Sugano energy level diagram. The calculated value of Dq/B is 2.47, indicating that Mn⁴⁺ is surrounded by a strong CF. Meanwhile, the calculated ²E_g energy level is 14 217–14 881 cm⁻¹ for LCH:xMn⁴⁺, which is in good agreement with our experimental result (14 437 cm⁻¹). This indicates that the result is reliable. At 150 °C, the integral intensity of LCH:0.002Mn⁴⁺ is only 0.416 times of that at 25 °C, originating from thermal quenching, which needs to be further improved by process optimization. The pc-WLEDs device is fabricated with 380 nm InGaN chip and the mixture of commercial blue BAM:Eu²⁺ phosphor, green (Ba, Sr)₂SiO₄:Eu²⁺ phosphor, and the LCH:0.002Mn⁴⁺ phosphor. The low CCT = 5165 K and high CRI ($R_a = 87.8$) mean that LCH:xMn⁴⁺ can be an excellent red-emitting phosphor for application in pc-WLEDs.

Conflicts of interest

The authors declare no competing financial interest.

Acknowledgements

This work is financially supported by the National Natural Science Foundation of China (NSFC No. 51672259).

References

- 1 C. C. Lin and R. S. Liu, *J. Phys. Chem. Lett.*, 2011, **2**, 1268–1277.
- 2 Z. Xia and Q. Liu, *Prog. Mater. Sci.*, 2016, **84**, 59–117.
- 3 L. Wang, R. J. Xie, T. Suehiro, T. Takeda and N. Hirotsuki, *Chem. Rev.*, 2018, **118**, 1951–2009.
- 4 G. Li, Y. Tian, Y. Zhao and J. Lin, *Chem. Soc. Rev.*, 2015, **44**, 8688–8713.
- 5 N. C. George, K. A. Denault and R. Seshadri, *Annu. Rev. Mater. Res.*, 2013, **43**, 481–501.
- 6 X. Qin, X. Liu, W. Huang, M. Bettinelli and X. Liu, *Chem. Rev.*, 2017, **117**, 4488–4527.
- 7 J. Zhong, W. Zhao, W. Zhuang, W. Xiao, Y. Zheng, F. Du and L. Wang, *ACS Omega*, 2017, **2**, 5935–5941.
- 8 N. C. George, A. J. Pell, G. Dantelle, K. Page, A. Llobet, M. Balasubramanian, G. Pintacuda, B. F. Chmelka and R. Seshadri, *Chem. Mater.*, 2013, **25**, 3979–3995.
- 9 J. Ueda, P. Dorenbos, A. J. J. Bos, A. Meijerink and S. Tanabe, *J. Phys. Chem. C*, 2015, **119**, 25003–25008.
- 10 D. Kuramoto, H. S. Kim, T. Horikawa, M. Itoh and K.-i. Machida, *J. Phys.: Conf. Ser.*, 2012, **379**, 012015.
- 11 H. S. Kim, K.-i. Machida, T. Horikawa and H. Hanzawa, *J. Alloys Compd.*, 2015, **633**, 97–103.
- 12 Y. Wang, Y. L. Wang, Y. R. Shao, M. Wang and Y. C. Zhu, *Mater. Technol.*, 2017, **32**, 845–851.
- 13 L. Huang, Y. Zhu, X. Zhang, R. Zou, F. Pan, J. Wang and M. Wu, *Chem. Mater.*, 2016, **28**, 1495–1502.
- 14 L. L. Wei, C. C. Lin, Y. Y. Wang, M. H. Fang, H. Jiao and R. S. Liu, *ACS Appl. Mater. Interfaces*, 2015, **7**, 10656–10659.
- 15 H. Lian, Q. Huang, Y. Chen, K. Li, S. Liang, M. Shang, M. Liu and J. Lin, *Inorg. Chem.*, 2017, **56**, 11900–11910.
- 16 M. H. Fang, C. S. Hsu, C. Su, W. Liu, Y. H. Wang and R. S. Liu, *ACS Appl. Mater. Interfaces*, 2018, **10**, 29233–29237.
- 17 Y. Y. Zhou, E. H. Song, T. T. Deng and Q. Y. Zhang, *ACS Appl. Mater. Interfaces*, 2018, **10**, 880–889.
- 18 H. Zhu, C. C. Lin, W. Luo, S. Shu, Z. Liu, Y. Liu, J. Kong, E. Ma, Y. Cao, R. S. Liu and X. Chen, *Nat. Commun.*, 2014, **5**, 4312.
- 19 Y. Zhu, Z. Qiu, B. Ai, Y. Lin, W. Zhou, J. Zhang, L. Yu, Q. Mi and S. Lian, *J. Lumin.*, 2018, **201**, 314–320.
- 20 M. Peng, X. Yin, P. A. Tanner, M. G. Brik and P. Li, *Chem. Mater.*, 2015, **27**, 2938–2945.
- 21 W. Lu, W. Lv, Q. Zhao, M. Jiao, B. Shao and H. You, *Inorg. Chem.*, 2014, **53**, 11985–11990.
- 22 J. Zhong, S. Zhou, D. Chen, J. Li, Y. Zhu, X. Li, L. Chen and Z. Ji, *Dalton Trans.*, 2018, **47**, 8248–8256.
- 23 G. Xing, Y. Feng, M. Pan, Y. Wei, G. Li, P. Dang, S. Liang, M. S. Molokeev, Z. Cheng and J. Lin, *J. Mater. Chem. C*, 2018, **6**, 13136–13147.

- 24 A. Fu, C. Zhou, Q. Chen, Z. Lu, T. Huang, H. Wang and L. Zhou, *Ceram. Int.*, 2017, **43**, 6353–6362.
- 25 H. Chen, H. Lin, Q. Huang, F. Huang, J. Xu, B. Wang, Z. Lin, J. Zhou and Y. Wang, *J. Mater. Chem. C*, 2016, **4**, 2374–2381.
- 26 R. Cao, Z. Shi, G. Quan, T. Chen, S. Guo, Z. Hu and P. Liu, *J. Lumin.*, 2017, **188**, 577–581.
- 27 K. Li, H. Lian and R. V. Deun, *J. Lumin.*, 2018, **198**, 155–162.
- 28 A. Fu, A. Guan, D. Yu, S. Xia, F. Gao, X. Zhang, L. Zhou, Y. Li and R. Li, *Mater. Res. Bull.*, 2017, **88**, 258–265.
- 29 R. Cao, X. Ceng, J. Huang, H. Ao, G. Zheng, X. Yu and X. Zhang, *Opt. Mater.*, 2016, **62**, 706–710.
- 30 R. Cao, X. Ceng, J. Huang, X. Xia, S. Guo and J. Fu, *Ceram. Int.*, 2016, **42**, 16817–16821.
- 31 S. Coh, T. Heeg, J. H. Haeni, M. D. Biegalski, J. Lettieri, L. F. Edge, K. E. O'Brien, M. Bernhagen, P. Reiche, R. Uecker, S. Trolier-McKinstry, D. G. Schlom and D. Vanderbilt, *Phys. Rev. B: Condens. Matter Mater. Phys.*, 2010, **82**, 064101.
- 32 S. KATO, T. ABE, M. SUGAI, H. TAKIZAWA and T. ENDO, *J. Ceram. Soc. Jpn.*, 1999, **107**, 633–638.
- 33 R. D. SHANNON, *Acta Crystallogr., Sect. A: Cryst. Phys., Diffr., Theor. Gen. Crystallogr.*, 1976, **32**, 751–767.
- 34 Z. Zhang, C. Ma, R. Gautier, M. S. Molokeev, Q. Liu and Z. Xia, *Adv. Funct. Mater.*, 2018, 1804150.
- 35 Y. Wei, L. Cao, L. Lv, G. Li, J. Hao, J. Gao, C. Su, C. C. Lin, H. S. Jang, P. Dang and J. Lin, *Chem. Mater.*, 2018, **30**, 2389–2399.
- 36 Y. Liu, J. Silver, R.-J. Xie, J. Zhang, H. Xu, H. Shao, J. Jiang and H. Jiang, *J. Mater. Chem. C*, 2017, **5**, 12365–12377.
- 37 X. Wang, Z. Zhao, Q. Wu, Y. Li and Y. Wang, *Inorg. Chem.*, 2016, **55**, 11072–11077.
- 38 G. Li, Y. Wang, W. Zeng, W. Chen, S. Han, H. Guo and Y. Li, *J. Mater. Chem. C*, 2016, **4**, 3304–3312.
- 39 G. Li, Z. Hou, C. Peng, W. Wang, Z. Cheng, C. Li, H. Lian and J. Lin, *Adv. Funct. Mater.*, 2010, **20**, 3446–3456.
- 40 X. Zhang, J. Nie, S. Liu, Y. Li and J. Qiu, *J. Am. Ceram. Soc.*, 2018, **101**, 1576–1584.
- 41 Mikhail G. Brika and A. M. Srivastava, *ECS J. Solid State Sci. Technol.*, 2013, **2**, R148–R152.
- 42 M. G. Brik and A. M. Srivastava, *J. Lumin.*, 2013, **133**, 69–72.
- 43 M. G. Brik, S. J. Camardello, A. M. Srivastava, N. M. Avram and A. Suchocki, *ECS J. Solid State Sci. Technol.*, 2016, **5**, R3067–R3077.
- 44 M. G. Brik and A. M. Srivastava, *ECS J. Solid State Sci. Technol.*, 2018, **7**, R3079–R3085.
- 45 M. G. Brik, S. J. Camardello and A. M. Srivastava, *ECS J. Solid State Sci. Technol.*, 2015, **4**, R39–R43.
- 46 M. Zhao, H. Liao, L. Ning, Q. Zhang, Q. Liu and Z. Xia, *Adv. Mater.*, 2018, 1802489.
- 47 Y. H. Kim, P. Arunkumar, B. Y. Kim, S. Unithrattil, E. Kim, S. H. Moon, J. Y. Hyun, K. H. Kim, D. Lee, J. S. Lee and W. B. Im, *Nat. Mater.*, 2017, **16**, 543–550.